Proc. Lunar Sci. Conf. 6th (1975), p. 2785–2796.
Printed in the United States of America

Farside lunar gravity from a mass point model

MOHAN ANANDA
Jet Propulsion Laboratory, Pasadena, California 91103

Abstract—A mass point representation of the lunar gravity field was determined from the long-periodic orbital variations of the Apollo 15 and 16 subsatellites and Lunar Orbiter V. A radial acceleration contour map, evaluated at 100 km altitude from the lunar surface, shows that the nearside is in close agreement with the result derived from the line of sight method by Muller and Sjogren. The farside map shows the highland regions as broad positive gravity anomaly areas and the basins such as Korolev, Hertzsprung, Moscoviense, Mendeleev, and Tsiolkovsky as localized, negative gravity anomaly regions. The farside map has a first-order agreement with the result derived from the harmonic field method by Ferrari. The mass points analysis indicates that the nearside is almost all negative gravity anomaly regions except for the known positive mass anomaly basins (mascons) and the farside is almost all positive gravity anomaly regions except for some localized negative areas near the basins.

THE APOLLO PROGRAM provided a vast amount of various types of lunar data. These data have led to models for the composition and structure of the interior of the moon, however information on the farside lunar gravity has never been incorporated. Several lunar gravity fields represented by spherical harmonic coefficients have been published (Lorell, 1970; Liu and Laing, 1971; Michael and Blackshear, 1972). Farside acceleration contours from these fields give unrealistic values and show no correlation between topography and gravity. The similarity between the various fields is minimal.

Since the discovery of "mascons" on the moon by Muller and Sjogren (1968), there has been much interest in modeling the gravity field by point masses or disks or lenses, instead of the conventional harmonic coefficient representation. The gravity map of the lunar nearside has been well determined by discrete mass point representations (Sjogren *et al.*, 1971; Wong *et al.*, 1971). The mass point representation has also been applied to the determination of the gravity field of Mars (Sjogren *et al.*, 1975), by processing the Mariner Mars 1971 orbiter tracking data. A long-periodic mass point modeling approach has been utilized in this analysis in processing the Apollo 15 and 16 subsatellites and Lunar Orbiter V data to determine the farside and nearside gravity field.

Apollo 15 and 16 subsatellites tracking data are completely thrust free and thus a large contiguous block of data was used in this analysis. About two years of tracking data for Apollo 15 subsatellite and 32 days of tracking data for Apollo 16 subsatellite are available for gravity field determination. Since both subsatellites are in low inclination orbits (Apollo 15 subsatellite, $i = 30°$, Apollo 16 subsatellite, $i = 10°$), a small segment of about 7 days of attitude-control-thrust-free Lunar Orbiter V ($i = 85°$) tracking data was also included in the data set. The addition of high inclination data has helped to separate the correlations between the mass

Table 1. Orbit data description.

Satellite	Period	Eccentricity	Inclination	No. of data* points	Data weights used			
					$\sigma_{\dot{e}}$†	$\sigma_{\dot{I}}$‡	$\sigma_{\dot{\Omega}}$‡	$\sigma_{\dot{\omega}}$‡
Apollo 15	2 hr	0.02	151°	238	0.25×10^{-9}	0.23×10^{-8}	0.27×10^{-8}	0.22×10^{-7}
Apollo 16	2 hr	0.02	170°	129	0.25×10^{-9}	0.23×10^{-8}	0.27×10^{-8}	0.22×10^{-7}
Lunar-Orbiter V	3 hr	0.28	85°	28	0.1×10^{-8}	0.28×10^{-8}	0.17×10^{-8}	0.41×10^{-8}

*4 data points/day are used.
†(/sec).
‡(rad/sec).

points. The inclusion of Lunar Orbiter IV data would have helped to get some separation by difference in altitude, but the Lunar Orbiter IV data which were processed seem to contain non-gravitational perturbations and thus this data was not used in this analysis. Table 1 contains pertinent information about these satellites.

The method of data reduction employed in this analysis is based on processing the long-periodic variations in the mean Keplerian orbital elements of the satellites. This approach is quite different from the method of directly fitting the doppler data. A similar approach has been used by Ferrari (1975), however his gravity field was represented by harmonic coefficients, rather than a grid of mass points.

The data reduction process was a two-stage approach. In the first stage, the raw doppler tracking data were reduced to obtain mean orbital elements (a, e, I, ω, Ω) for each orbit. A low order lunar gravity model* and the perturbations due to earth, sun, and solar radiation pressure were used in processing the raw doppler tracking data. The mean elements were spline fit and the time derivatives were generated. Analysis indicated that the smoothing process by spline fitting has not introduced any substantial errors and these seem to be well within the noise level of the mean elements. In the second stage the gravity parameters (point masses) were determined by fitting the time derivatives of the mean orbital elements ($\dot{e}$, $\dot{I}$, $\dot{\omega}$, $\dot{\Omega}$). As there is no long-periodic variation in semi-major axis (a) due to gravity perturbation, the mean element a was not used in the data reduction. The variation in mean a is less than 300 m. The data were corrected for all non-lunar gravity perturbations, such as earth, sun, and solar radiation pressure effects (Lorell and Liu, 1971; Kozai, 1961). The data were also adjusted for the second harmonic of the gravity field ($J_2 = .204\times10^{-3}$).

To demonstrate that the farside gravity anomalies can be recovered from the nearside doppler data a simulation study was performed. In the simulation study, surface mass disks were placed both on the nearside and farside of the moon and trajectories were integrated from a given set of initial conditions. Simulated

*The harmonic coefficients of the reference model are $J_2 = .207108\times10^{-3}$, $C_{22} = .207\times10^{-4}$, $J_3 = -.21\times10^{-4}$, $C_{31} = .35\times10^{-4}$, $C_{33} = .258\times10^{-5}$.

doppler tracking data were computed, along the direction of observation from the earth, throughout the orbit as if one could see through the moon. A set of mean orbital elements were computed by fitting the doppler data all around the orbit (the orbital period is approximately 120 min). Similarly various sets of mean orbital elements were computed by fitting doppler data along partial orbits (50, 60, and 69.5 min of data). The partial fit mean elements compared well to those from the mean elements generated by fitting the complete orbit. The mean elements generated by fitting data from the nearside partial orbits were compared against the mean elements generated by fitting data from the farside partial orbits. The mean elements were not sensitive to the fact that the data was taken from the nearside partial orbits or the farside partial orbits.

Figure 1 shows the variation of eccentricity as a function of the number of orbits. This variation is computed by numerically differencing the mean eccentricities of the adjacent orbits. The continuous curve corresponds to the variation in eccentricity obtained by fitting the complete orbit (120 min). The triangles, circles, and squares correspond to variations in eccentricities obtained by fitting the partial orbits of 69.5, 60, and 50 min, respectively. It is seen here that the difference between the variations in eccentricity generated by fitting the complete data and the partial data of 69.5 or 60 min is negligible. However, the variations in eccentricity obtained by fitting 50 min of data are much different. Thus it is shown that the variations in mean elements of the orbit can be determined by fitting the data along half or more of the orbit.* This simulation study thus indicated that the

*The simulation study was performed with the help of W. L. Sjogren. I am also indebted to John Smith for his programming support for this simulation study.

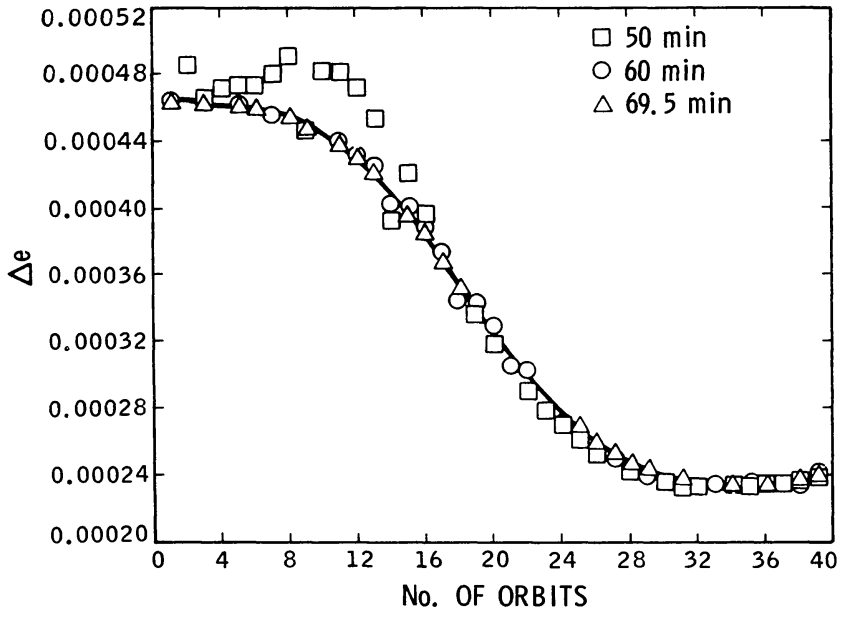

Fig. 1. Variations in eccentricity as determined by partial tracking coverage.

long-periodic variations in mean elements generated by fitting the nearside data alone could yield gravity anomaly parameters of the farside.

A discrete point mass model was employed in this analysis to determine the farside and nearside lunar gravity field by reducing Apollo 15 and 16 subsatellites data and Lunar Orbiter V data. The mathematical model in processing the data was developed by averaging the partial derivatives of the disturbing potential due to a point mass with respect to the orbital elements, and substituting these partials into the variations of parameters equations (Ananda, 1975). In processing the data, the mass points were distributed such that the locations were *a priori* fixed. Only the mass values were estimated. As the Apollo 15 and Apollo 16 subsatellites data dominated over the Lunar Orbiter V data, the major data sensitivity was in the region of $\pm 30°$ about the equator. Thus, the mass points were distributed such that each mass point was placed about 12–18° (450 km) apart over the region of $\pm 30°$ about the equator and 50 km below the lunar surface.

In order to select the depth at which to place the mass point, a simulation analysis was performed. A single mass point was placed at various depths (25, 50, 100, and 150 km) and the variations in the rate of mean eccentricity was computed over several days. A trajectory similar to Apollo 15 subsatellite was assumed for the study. The signature of the eccentricity rate over the time period was sensitive to the depth at which the mass point was placed. Figure 2 shows a typical case. A similar analysis was done by placing a 170-km radius disk at the lunar surface.

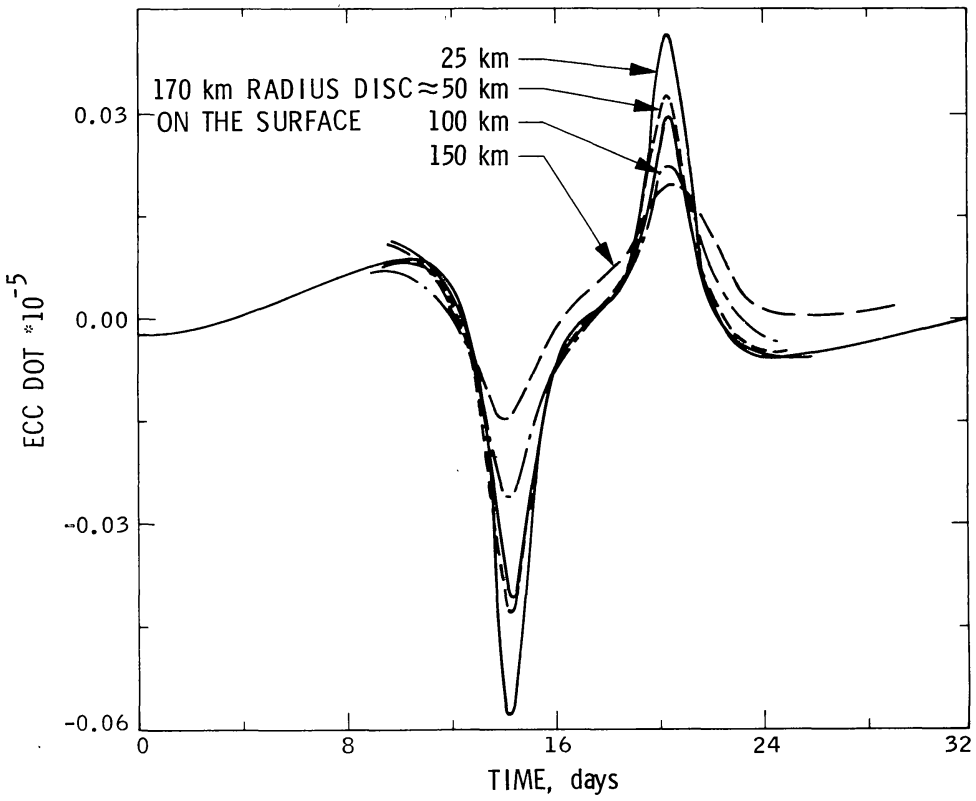

Fig. 2. Eccentricity variations as mass depths.

This disk represented the Humorum Basin which is about 170 km in radius. The analysis indicated that the signature generated by the disk placed on the lunar surface and the signature generated by the point mass placed 50 km below the lunar surface were close in amplitude and frequency. For example, the rms error in $\dot{e}$ fit is less than $.1 \times 10^{-8}$. Thus as an average all of the mass points in this analysis were placed 50 km below the mean lunar surface.

The mass points were distributed such that the correlations between them were minimized. This was achieved by analyzing the ground track of Apollo 15 and 16 subsatellites and care was taken not to place two or more mass points on one orbital path. Thus the mass points were not uniformly distributed. Moreover, after performing data reduction with a certain number of mass points, some were removed from the original set to eliminate high pair correlations (correlation coefficients of more than 0.6) which produced unrealistic results.

In a multiparameters system even relatively low pairwise correlations may be symptomatic of higher order linear combinations among the parameters. In this analysis, the correlation coefficients of 0.6 and more were observed to lead to results which were unacceptable. Singular value analysis was performed on this solution to study the singular value spread and results showed that the ratio between the largest and the smallest components was 10^6.* Thus the full rank or standard least-squares solution was numerically acceptable and there was no need to consider less than full rank solutions. (In fact singular value analysis on the original model gave condition numbers of 10^{17} which demonstrated numerical instability.)

In analyzing 60 days of Apollo subsatellite data, about 32 days of Apollo 16 subsatellite data and about 7 days of Lunar Orbiter V data, estimates of 117 mass points were obtained. There were four data points in each day totaling 395 data points (1580 Keplerian rates) altogether. The data sets were kept separate and the combinations were processed with different weighting factors and the data weights are given in Table 1. A weighted least-squares filtering algorithm was employed in reducing the data. A square-root form of the filtering equations was used in the data processing scheme to enhance the numerical stability of the solution (Bierman, 1973). About 90% of the information has been extracted from the data and the residuals show systematic signatures indicating the effect of unmodeled gravity parameters. The mass estimates of the 117 mass points and their locations (latitude and longitude) and the standard deviation in the estimates are given in Table 2. The point masses have been transformed into harmonic coefficients and the low order and degree coefficients agree to first order with the coefficients published by Sjorgen (1971). However, the first degree and order terms (C_{11} and S_{11}) are not identically zero, indicating that the center of mass of the system has been displaced about 200 m off the center of the coordinate system. The solution obtained here did not make use of the constraints that the

*The exponent is inversely related to the number of digits accuracy one can expect (i.e. N – exponent $\approx$ the number digits of accuracy, where N is the number of digits in the mantissa of the computer generated numbers).

Table 2. Mass point location value and standard deviation.

Mass point number	Longitude (deg.)	Latitude (deg.)	Mass value parts/total mass*	Std. dev. parts/total mass
1	−180	26	.0186	.0011
2	−160	26	.0291	.0010
3	−140	26	−.0042	.0010
4	−120	26	.0035	.0010
5	−100	26	−.0284	.0009
6	−80	26	.0029	.0009
7	−60	26	.0349	.0008
8	−40	26	−.0436	.0008
9	−20	26	.0033	.0007
10	00	26	−.0122	.0007
11	20	26	.0661	.0006
12	60	26	−.0176	.0007
13	80	26	.0071	.0010
14	100	26	−.0820	.0008
15	120	26	.0345	.0009
16	140	26	.0533	.0009
17	160	26	−.0372	.0010
18	−170	14	.0598	.0006
19	−150	14	.0005	.0006
20	−130	14	.0453	.0006
21	−110	14	−.0047	.0006
22	−90	14	−.0204	.0006
23	−75	14	.0397	.0007
24	−60	14	−.0285	.0005
25	−45	14	−.0199	.0005
26	−10	14	−.0009	.0005
27	10	14	−.0195	.0004
28	30	14	−.0149	.0005
29	45	14	−.0402	.0006
30	75	14	.0169	.0006
31	90	14	−.0509	.0006
32	110	14	−.0285	.0005
33	130	14	.0264	.0005
34	150	14	.0294	.0007
35	170	14	−.0445	.0007
36	−177	3	.0126	.0004
37	−165	3	.0346	.0003
38	−145	3	.0329	.0003
39	−130	3	−.0220	.0004
40	−110	3	.0059	.0003
41	−90	3	.0292	.0004
42	−75	3	−.0216	.0003
43	−55	3	−.0108	.0003
44	−35	3	−.0268	.0003
45	−20	3	.0121	.0002
46	00	3	.0001	.0002
47	20	3	.0157	.0002

Table 2. (*Continued*).

Mass point number	Longitude (deg.)	Latitude (deg.)	Mass value parts/total mass*	Std. dev. parts/total mass
48	40	3	−.0362	.0002
49	60	3	−.0194	.0002
50	80	3	−.0395	.0003
51	95	3	−.0359	.0003
52	115	3	.0016	.0003
53	135	3	−.0146	.0004
54	150	3	.0140	.0004
55	170	3	−.0068	.0004
56	−168	−7	.0424	.0004
57	−150	−7	.0401	.0004
58	−132	−7	.0109	.0004
59	−114	−7	.0072	.0004
60	- 96	−7	.0371	.0004
61	−78	−7	−.0138	.0004
62	−60	−7	−.0095	.0003
63	−42	−7	−.0168	.0003
64	−24	−7	−.0204	.0004
65	−6	−7	−.0070	.0003
66	12	−7	−.0383	.0003
67	30	−7	.0031	.0003
68	48	−7	−.0155	.0003
69	66	−7	−.0257	.0003
70	102	−7	.0123	.0004
71	120	−7	.0212	.0004
72	138	−7	.0506	.0003
73	156	−7	.0267	.0003
74	174	−7	.0546	.0004
75	−180	−17	−.0083	.0005
76	−162	−17	.0209	.0005
77	−144	−17	−.0015	.0005
78	−126	−17	.0041	.0006
79	−108	−17	−.0086	.0006
80	− 90	−17	−.0271	.0006
81	−72	−17	−.0177	.0005
82	−54	−17	.0033	.0004
83	−36	−17	.0045	.0004
84	−18	−17	−.0104	.0005
85	00	−17	.0091	.0004
86	18	−17	−.0128	.0005
87	36	−17	.0348	.0004
88	54	−17	−.0362	.0005
89	72	−17	−.0076	.0005
90	90	−17	−.0106	.0005
91	108	−17	−.0097	.0005
92	126	−17	−.0333	.0005
93	144	−17	−.0037	.0006
94	162	−17	.0367	.0005

Table 2. (*Continued*).

Mass point number	Longitude (deg.)	Latitude (deg.)	Mass value parts/total mass*	Std. dev. parts/total mass
95	−168	−26	.0099	.0008
96	−150	−26	−.0037	.0008
97	−132	−26	−.0077	.0008
98	−114	−26	−.0164	.0008
99	−96	−26	.0393	.0007
100	−78	−26	−.0343	.0006
101	−6	−26	−.0119	.0005
102	12	−26	.0142	.0006
103	30	−26	−.0123	.0005
104	48	−26	−.0212	.0006
105	66	−26	.0241	.0007
106	84	−26	−.0355	.0007
107	102	−26	.0248	.0008
108	120	−26	−.0357	.0008
109	138	−26	−.0073	.0008
110	156	−26	.0559	.0007
111	174	−26	−.0117	.0007
112	−19	37	.0241	.0008
113	59	17	.0467	.0005
114	−39	−24	.0034	.0004
115	−8	10	.0241	.0003
116	84	−3	.0146	.0003
117	−95	−20	.0363	.0007

*GM value = 4902.78 km^3/sec^2.

total sum of the point masses is zero and the center of mass and center of the coordinate system coincide.

A radial acceleration map, evaluated at 100-km altitude from the lunar surface, has been generated for the 117 mass points. Different sets of mass point solutions (115, 119, and 121 point masses) have also been obtained and the radial acceleration maps generated. The general shape of the contours remain about the same in all the maps, thus giving confidence in the solutions. Figure 3 shows the nearside radial acceleration contours for the 117 mass point solution, and Fig. 4 shows the farside radial acceleration contours relative to a J_2 acceleration surface. The nearside is in close agreement with the result derived from the line-of-sight method (Muller and Sjogren, 1968). The 117 mass point model resolves all the previously known mascons (Mare Imbrium, Mare Serenitatis, Mare Crisium, Mare Nectaris, Mare Humorum, Mare Smythii, and Sinus Aestuum) as positive gravity anomaly regions. The central highland regions are resolved as positive gravity anomaly regions. The areas near Oceanus Procellarum, Mare Tranquilitatis, and Mare Fecunditatis are all resolved as negative gravity anomaly regions. Mare Orientale is resolved as a strong positive anomaly. Though the basin Mare Imbrium

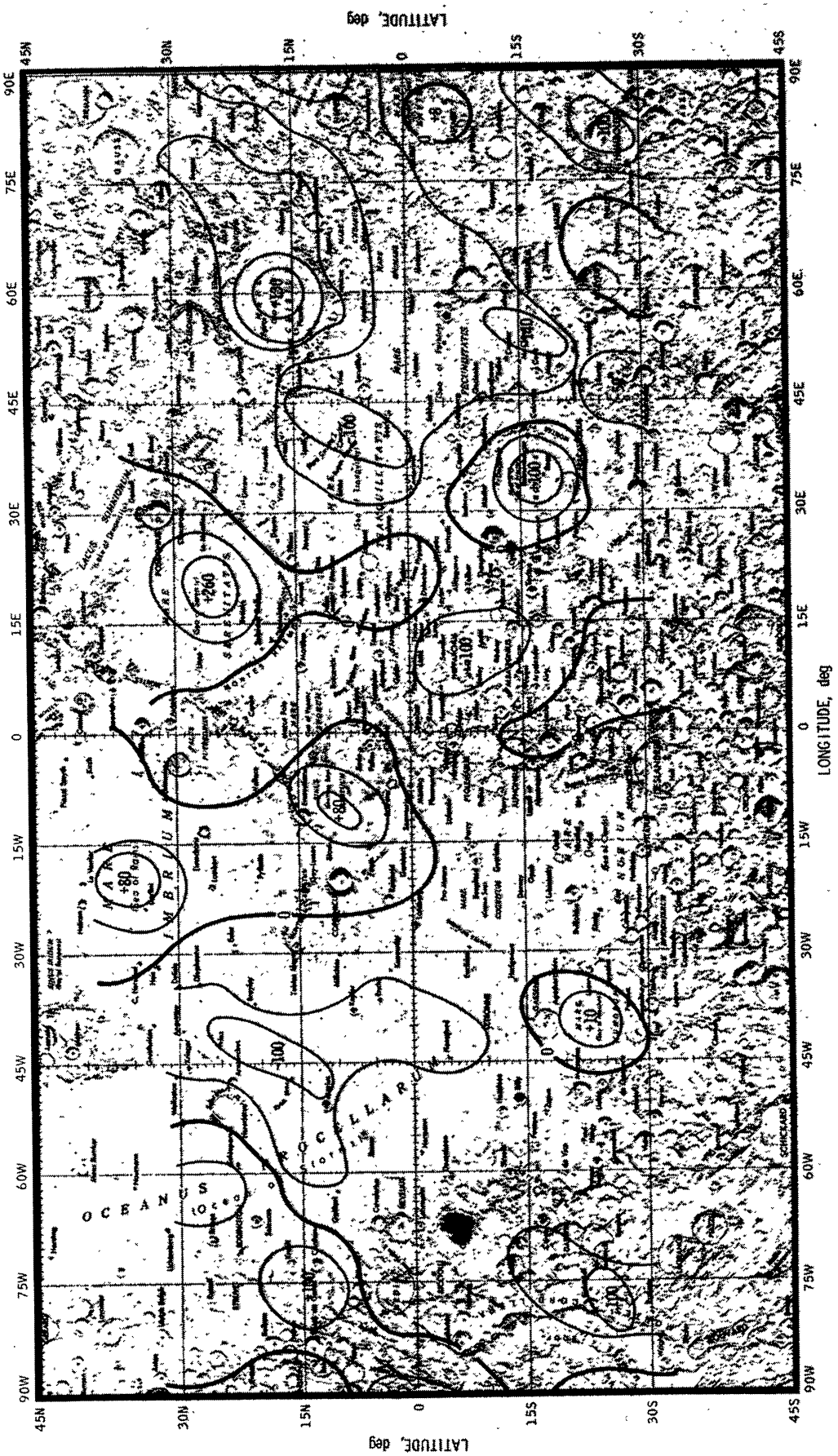

Fig. 3. Lunar gravity field (nearside) milligals at 100 km above surface.

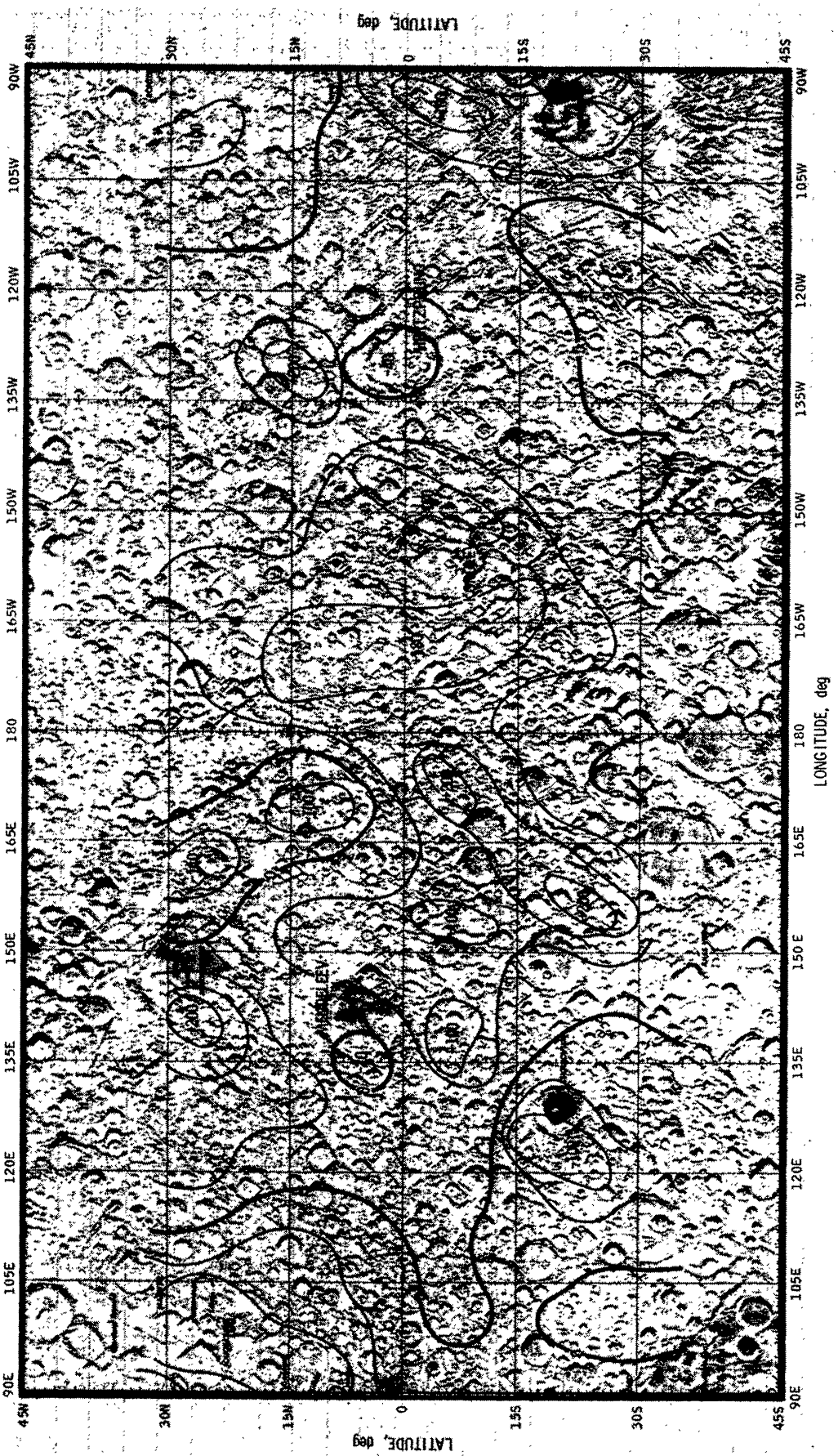

Fig. 4. Lunar gravity field (farside) milligals at 100 km above surface.

is resolved to be a positive gravity anomaly region the magnitude (+80 milligals) is not as large as the one obtained by the line of sight method (over 200 milligals). This is because the anomaly is at about +37° latitude and the Apollo 15 and 16 subsatellite data coverage is only up to +30° in latitude. In general, the nearside seems to be all negative gravity anomaly regions except for the known positive mass anomaly basins. Note, however the effect of J_2 has been removed and its addition would be approximately 50 milligals at the equator.

The lunar farside gravity map shows the highland regions as broad positive gravity anomaly areas and the basins such as Korolev, Hertzsprung, Moscoviense, Mendeleev, and Tsiolkovsky as localized negative gravity anomaly regions. In general the farside is almost all positive gravity anomaly regions except for some localized negative areas near the basins. The basin Korolev seems to lie between two gravity high regions whereas the basin Hertzsprung resolves as a localized negative gravity anomaly area. There exists a large basin starting 25°S in latitude around 180° longitude and the gravity anomaly seems to change from positive to negative in that area. As the data coverage does not go below 30°S the gravity parameters below 30°S latitude were not resolved.

The farside basins do not exhibit positive gravity anomalies as in the cases of nearside basins. Thus no new "mascons" were discovered on the farside. The farside basins are not maria filled whereas the nearside basins are maria filled. Thus maria fillings seem to be highly correlated with basins having gravity highs. The farside regions exhibit correlation with topography generated from the Apollo laser altimetry (Sjogren and Wollenhaupt, 1973). The farside basins are resolved as localized negative anomalies whereas the highland regions are resolved as broad positive gravity anomaly regions.

The farside gravity map has a first order agreement with the results derived from the spherical harmonic coefficients method (Ferrari, 1975). Further studies will continue by combining low degree harmonic coefficients and discrete mass points to model the lunar gravity field. In addition, solutions will be derived which constrain the center of mass and the total mass of the point mass model.

Acknowledgments—I wish to thank W. L. Sjogren for his valuable suggestions and Ray Wimberly and Nancy Hamata for their computational support.

References

Ananda M. P. (1975) Mean rates of the orbital elements of a satellite perturbed by a lens shaped mass concentration. *Celestial Mechanics.* In press.

Bierman G. J. (1973) Comparison of discrete linear filtering algorithms. *IEEE Transactions on Aerospace and Electronic Systems* **AES 9**(1), 22–27.

Ferrari A. J. (1975) Lunar gravity: The first farside map. *Science.* In press.

Kozai Y. (1961) Effects of solar radiation pressure on the motion of an artificial satellite. Smithsonian Institute Report No. 56, p. 25–34.

Liu A. S. and Laing P. A. (1971) Lunar gravity analysis from long term effects. *Science* **173**, 1017–1020.

Lorell J. (1970) Lunar orbiter gravity analysis. *The Moon* 3, 190–231.

Lorell J. and Liu A. S. (1971) Method of averages expansion for artificial satellite application. JPL Report 32–1513, p. 18.

Michael W. H., Jr. and Blackshear W. T. (1972) Recent results on the mass gravitational field and moments of inertia of the moon. *The Moon* **3**, 388–402.

Muller P. M. and Sjogren W. L. (1968) Mascons: Lunar mass concentrations. *Science* **161**, 680–684.

Muller P. M. and Sjogren W. L. (1969) Lunar gravimetry and mascons. *Appl. Mech. Rev.* **22**(9), 955–959.

Sjogren W. L. (1971) Lunar gravity estimate: Independent confirmation. *J. Geophys. Res.* **76**, 7021–7026.

Sjogren W. L. and Wollenhaupt W. R. (1973) Lunar shape via the Apollo laser altimeter. *Science* **179**, 275–278.

Sjogren W. L., Muller, P. M., Gottlieb P., Wong L., Buechler G., Downs. W., and Prislin R. (1971) Lunar surface mass distribution from dynamical point mass-solution. *The Moon* **2**, 338–353.

Sjogren W. L., Lorell J., Wong L., and Downs W. (1975) Mars gravity field based on a short arc technique. *J. Geophys. Res.* In press.

Wong L., Buechler G., Downs W., Sjogren W., Muller P., and Gottlieb P. (1971) A surface-layer representation of the lunar gravitational field. *J. Geophys. Res.* **76**, 6220–6236.